

The radiative torque spin-up efficiency of ballistic dust grain aggregates

Jonathan A. Jäger¹, Stefan Reissl¹, and Ralf S. Klessen^{1,2}

¹ Universität Heidelberg, Zentrum für Astronomie, Institut für Theoretische Astrophysik, Albert-Ueberle-Straße 2,
D-69120 Heidelberg, Germany

² Universität Heidelberg, Interdisziplinäres Zentrum für Wissenschaftliches Rechnen, Im Neuenheimer Feld 205,
D-69120 Heidelberg, Germany

July 16, 2024

ABSTRACT

Aims. Understanding the rotational dynamics of interstellar dust grains is quintessential for the analysis of the observed dust polarization signal. We aim to constrain the set of parameters for an accurate description of the rotational spin-up process of ballistic dust grain aggregates driven by radiative torques (RATs).

Methods. We model the dust grains as complex fractal aggregates grown by the ballistic aggregation of uniform spherical particles (monomers) of different sizes. A broad variation of dust materials, shapes, and sizes are studied in the presence of different radiation sources.

Results. We find that the canonical parametrization for the torque efficiency overestimates the maximal angular velocity ω_{RAT} caused by RATs of grain aggregates, and to resolve this problem we propose a new parametrization which predicts ω_{RAT} more accurately. We find that RATs are strongest for larger grains with smaller monomer-density, this manifests as size and monomer-density dependence in the constant part of the parametrization. Following the constant part, the parametrization has two power-laws with different slopes, which retain the universality for all grain sizes. The maximum grain rotation does not scale linearly with radiation strength, due to different drag mechanisms dominating depending on grain material and environment. The angular velocity ω_{RAT} of individual single dust grains has a wide distribution and may even differ from the mean by up to two orders of magnitude.

Key words. dust, microphysics, radiative torques, rotation, ballistic aggregates, RAT, porosity, alignment, spin-up

1. Introduction

Dust is a common component in astronomic environments, from galaxies to stellar discs and therefore plays a crucial role in observations. Most astronomers come into contact with dust because of dust extinction, which affects almost all observations (Draine 2003). Calzetti et al. (2000) as well as Bernstein et al. (2002) estimated, that 30 % or more of the energy produced by stars in the universe is absorbed by dust and re-emitted in the infrared. The dust helps to cool down gas, facilitating gravitational collapse (Omukai et al. 2005), also playing a major role in later stages of star formation, as well as constituting the first stage in the formation of planets (Dullemond et al. 2008; Liu & Ji 2020). Rapidly rotating dust grains are the common source for polarized light, carrying information about the magnetic field orientation (see e.g. Lazarian 2007; Andersson 2015, for review). The catalysis of molecular hydrogen (Hollenbach & Salpeter 1971; Cazaux & Tielens 2002) and other astrochemical reactions in the ISM (Dishoeck 2014) is also impacted by grain rotation (Hoang & Tram 2020). The first models trying to explain the observed dust alignment, like paramagnetic relaxation (Davis & Greenstein 1951) or the Gold mechanism (Gold 1952) both encountered problems and were ultimately unable to account for the observed alignment. A big leap in the study of alignment was made, when Purcell (1979) realized, that grains could experience systematic torques acting in a specific direction in grain coordinates for large time spans compared to the timescale it takes gas collisions to randomize the grain rotation. With such systematic

torques the grain can spin up to much faster angular velocities than the typical thermal rotation rate. With suprathermal rotation, a grain can remain in a given orientation for much longer than the gas collision timescale, allowing alignment of angular momentum with the maximal moment of inertia via inelastic relaxation or the Barnett relaxation discovered by Purcell (1979), based on the Barnett. (1917) effect, which causes magnetization along the rotation axis in a paramagnetic body. If the grains rotation axis is not aligned with a principal axis of inertia, the rotation axis and therefore the magnetisation axis will precess in body coordinates, dissipating energy and aligning the rotation axis with the axis of maximal moment of inertia. In the presence of an external magnetic field the Davis-Greenstein-process can align the grain with the magnetic field (Purcell 1979).

A one to one mapping of dust alignment to magnetic field lines would of course be of great use to the study of magnetic fields. Polarization observations of the object in question could then always be used to obtain information about the magnetic field morphology. However uncertainties about the completeness of the model remained e.g. no increase in polarization with extinction in cold dark clouds (Goodman et al. 1995) and alignment of grains in cometary dust (Harwit & Vanýsek 1971), so the exploration of other alignment mechanisms continued.

The idea of systematic radiative torques (RATs) as the cause for rapid grain rotation had already been advanced decades prior (Dolginov 1972; Dolginov & Mytrophanov 1976), but only became an integral part of dust alignment theory with the work of Draine & Weingartner (1996). Using the discrete dipole ap-

proximation (DDA) method it was shown, that scattering and absorption of light from irregular grains results in torques acting on timescales much larger than random gas collisions. Their calculations were done on a irregular shape of intersecting cuboids and it was found, that radiative torques depend strongly on grain size. Additional grain shapes were investigated in the following work (Draine & Weingartner 1997) in the context of anisotropic radiation, H_2 -formation torques and paramagnetic relaxation. In most cases the grain reaches long-term stable conditions by aligning the grains principal axis with the magnetic field. Later, Lazarian & Hoang (2007) (LH07 hereafter) introduced an analytic model (AMO) for a spherical grain attached to a flat rectangular mirror via a weightless non interacting rod in this way capturing the helical properties of irregular grains. The AMO was compared to DDA simulations of irregular grain models, corresponding to the grain shapes in Draine & Weingartner (1997) and found a good agreement. The alignment of grains principal axis with the direction of incoming radiation was confirmed when magnetic field effects were subdominant. The parametrization of the RAT spin-up efficiency was found to be a power-law with an exponent of about -3 . Physical implications of RATs were explored in following studies (Lazarian & Hoang 2008; Hoang & Lazarian 2008, 2009, 2016) and the model was expanded by the addition of superparamagnetic relaxation due to iron inclusions. This increased the range of parameters in which grains can efficiently align with the magnetic field which is necessary to explain high degrees of polarization from observations (Planck Collaboration et al. 2020). The AMO was used successfully to model synthetic dust polarization observations, as long as free alignment parameters could be used to adjust the model (Bethell et al. 2007; Hoang & Lazarian 2014; Reissl et al. 2016). Herranen et al. (2019) then made a step towards testing more realistic grain shapes: gaussian ellipsoids, oblate spheroids, prolate spheroids, and spheres with random deformations and found a shallower slope of -2.6 for the power-law for the RAT parametrization. In this work we take one more step towards more realistic grain shapes, by simulating random typically fractal aggregate grains composed of different sized monomers and compare their RATs to previous results. The motivation is to model the grain growth ab-initio using the current understanding, that dust is originally formed in AGB stellar winds or supernovae (Todini & Ferrara 2001; Schneider et al. 2014; Nanni et al. 2013). As the dust forming materials in the winds cool down, heavy elements condense into spherical particles - in the following called monomers - which are the building blocks for larger dust grains formed by monomer accretion and coagulation of grains (Gobrecht et al. 2016; Norris et al. 2012). More realistic grain modeling may result in differing interactions with radiation. One example being the study of Arnold et al. (2019), that found significant differences in dust blowout sizes between compact and agglomerated grains.

The aim of this work is to improve the understanding of RATs by simulating individual grains composed of monomers for different sources of radiation. The theoretical basis for our simulations and models for the sources are presented in Sect. 3. The properties of grains and the way they are modeled is presented in Sect. 2, usage of the simulation codes is explained in Sect. 5, results are shown in Sect. 6 and discussed in Sect. 7, a summary and outlook are given in Sect. 8.

2. Ballistic dust grain aggregation

In this work dust grains are modeled as conglomerates made up of spherical particles of a single material, called monomers. The monomers stay attached to each other due to the intermolecular forces at their contact area (see e.g. Johnson et al. 1971). The growth of larger dust grains follows an aggregation process by means of ballistic collision and sticking of individual monomers (Dominik & Tielens 1997). To mimic the grain growth process of ballistic aggregation (BA) we follow the procedure as outlined in Shen et al. (2008) modified to work with monomers of variable sizes (Reissl et al. 2023). Starting with two or three connected monomers new monomers with radii drawn from a log-normal distribution between 10 nm and 100 nm are injected into the simulation volume from random directions, sticking to the grain upon collision.

Grains with an effective radius a_{eff}^1 from 50 nm up to 250 nm in steps of 50 nm are created. To reach an exact effective radius the sizes of the final monomers added to the grain are sampled in a biased way (lowering the upper bound on monomer size), until the desired a_{eff} is exactly reached. In addition to BA where each monomer remains at its initial sticking position, we model different monomer-densities or porosities of aggregates by means of monomer migration. After hitting the forming grain the added monomer rolls along the surface of the monomer it impacted until it touches a second monomer of the grain (BAM1). Here, all monomers are connected to at least two other monomers. For the BAM2 case each monomer rolls twice until it touches a third monomer. For BAM2, all monomers are connected to at least three other monomers. This is the most dense a random grain can be packed with monomers using the migration process. It follows, that BA-grains are the least dense/most porous and BAM2-grains are the most dense/least porous, an exemplary grain of each monomer-density is shown in Fig. 1.

To recapitulate the three grain properties are: the material from which the grain is made (astrosilicate or hydrogenated amorphous carbon) which differ in their optical properties, the monomer-density of the grain (BA, BAM1, BAM2) determining how closely monomers are packed and finally grain size given by the effective radius (50 nm to 250 nm in steps of 50 nm). For every combination of these three properties 30 different grains are created, leading to a total of 900 individual grains. This method of modeling ballistic grain aggregates was previously used in Reissl et al. (2022).

3. Maximal grain rotation

In the presence of a directed radiation field, irregularly shaped dust grains can experience momentum transfer from photon-interactions. In general the time averaged forces acting on such a grain may result in a net-torque, accelerating the rotation. This radiative torque (RAT) can be evaluated by (see e.g. Draine & Weingartner 1996, and LH07)

$$\Gamma_{\text{RAT}} = \frac{1}{2} \gamma a_{\text{eff}}^2 \int \lambda u_{\lambda} Q_{\Gamma} d\lambda, \quad (1)$$

where γ describes the anisotropy of the radiation field, λ is the wavelength and the quantity $u_{\lambda} = F_{\lambda}/c$ is the spectral energy density of a radiation field with the spectral flux F_{λ} , whereas c is the speed of light. These factors determine the overall strength of the torque independent of grain shape and orientation.

¹ The effective grain radius gives the radius of the grain if it was reshaped into a perfect sphere.

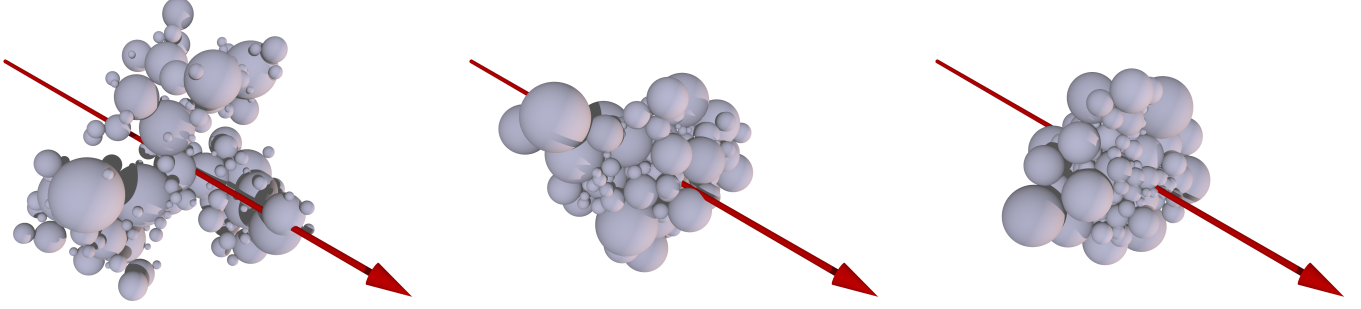


Fig. 1: Exemplary BA (left), BAM1 (middle), BAM2 (right) grains, respectively, with an effective radius of $a_{\text{eff}} = 250$ nm. The rotation axis \hat{a}_1 is depicted as a red arrow and is associated with the direction of the maximal moment of inertia I_{max} .

The effect of the individual grain shape and material is contained within the dimensionless spin-up efficiency vector \mathbf{Q}_Γ of the RAT. A perfectly spherical grain would experience no net torque at all, due to the symmetry between individual collisions resulting in clockwise or anticlockwise torques. However, for grains with irregular shapes, the contributions of individual radiation-dust interactions in a nonzero \mathbf{Q}_Γ vector, which modulates the orientation i.e. the sign as well as the magnitude of $\mathbf{\Gamma}_{\text{RAT}}$. In previous works a power-law parametrization for $\mathbf{Q}_\Gamma = |\mathbf{Q}_\Gamma|$ was suggested (LH07)

$$Q_\Gamma = \begin{cases} 0.4 & \text{if } \lambda \leq 1.8a_{\text{eff}} \\ 0.4 \left(\frac{\lambda}{1.8a_{\text{eff}}} \right)^\alpha & \text{otherwise} \end{cases} \quad (2)$$

In this paper we refer to this relation as the canonical parametrization. Here, the constant part transitions into a power-law at wavelengths equal to 1.8 times the effective radius of the grain. The power-law exponent typically lies between $\alpha = -2.6$ (Herranen et al. 2019) and $\alpha = -4$ (LH07).

For our grain dynamics modelling we assume stable alignment of the grains rotation with the direction of incoming radiation. For a single grain stably rotating about its principal axis the maximal possible angular momentum ω_{RAT} caused by RATs can be calculated as

$$\omega_{\text{RAT}} = \frac{\tau_{\text{drag}} \Gamma_{\text{RAT}}}{I_{\text{max}}} \quad (3)$$

where τ_{drag} is the drag-timescale and I_{max} is the largest moment of inertia, defining the a_1 -axis in the body-centric system of the grain (see e.g. Draine & Weingartner 1996, as well as Fig. 1). The total drag acting on the grain is composed of the collisions with the surrounding gas and the loss of angular momentum by emitting infrared photons. The total drag-timescale can be evaluated from the gas-drag-timescale τ_{gas} and photon-drag-timescale τ_{IR} with

$$\tau_{\text{drag}} = \frac{1}{\tau_{\text{gas}}^{-1} + \tau_{\text{IR}}^{-1}} \quad (4)$$

where a shorter timescale results in a stronger drag. Here, the gas-drag-timescale

$$\tau_{\text{gas}} = \frac{I_{\text{max}}}{n_{\text{gas}} m_{\text{gas}} v_{\text{th}} a_{\text{eff}}^4 Q_{\text{gas}}} \quad (5)$$

	$n_{\text{gas}} [\text{m}^{-3}]$	$T_{\text{gas}} [\text{K}]$
ISM	$5 \cdot 10^7$	100
AGN	$5 \cdot 10^7$	$5 \cdot 10^4$

Table 1: Fiducial gas parameters for the considered environments.

depends on the number density of the gas n_{gas} as well as the gas mass m_{gas} per particle and the mean thermal velocity v_{th} of the gas (see e.g. Draine & Weingartner 1996). The shape of the grain has an impact on the gas drag, with some shapes increasing the ability of the gas to exert torque on the grain. This influence of grain shape is quantified by the dimensionless gas-drag-efficiency Q_{gas} . We explore two environments with the same gas number densities n_{gas} and different temperatures T_{gas} as listed in Tab. 1. The photon-drag-timescale

$$\tau_{\text{IR}} = \frac{c^2 I_{\text{max}}}{a_{\text{eff}}^2 f_{\text{IR}}(T_{\text{dust}})} \quad (6)$$

depends on the integral over the photon emission

$$f_{\text{IR}}(T_{\text{dust}}) = 4\pi \int_0^\infty \lambda^2 B_\lambda(T_{\text{dust}}) Q_{\text{abs}}(\lambda) d\lambda \quad (7)$$

Here, $B_\lambda(T_{\text{dust}})$ is the Planck function modulated by the dimensionless efficiency of absorption $Q_{\text{abs}}(\lambda)$, where as T_{dust} is the dust temperature. For simplicity, the dust is illuminated by a single source without extinction. For the dust heating we assume thermal equilibrium. Therefore, the temperature of a single dust grain can be evaluated via

$$\int_0^\infty F_\lambda Q_{\text{abs}}(\lambda) d\lambda = 4\pi \int_0^\infty B_\lambda(T_{\text{dust}}) Q_{\text{abs}}(\lambda) d\lambda \quad (8)$$

by equating the source flux F_λ absorbed by the grain with the characteristic emitted flux $B_\lambda Q_{\text{abs}}(\lambda)$ of each grain.

4. The radiation field

Typical sources of radiation are chosen to evaluate the RATs they cause by irradiating the grains. Among the different sources are

	$R [R_{\odot}]$	$T_{\text{eff}} [\text{K}]$	$L_{\text{bol}} [L_{\odot}]$	γ	$u [u_{\text{ISRF}}]$
ISRF	-	-	-	0.1	1.0
S1	50	$1.5 \cdot 10^4$	$4.6 \cdot 10^5$	0.7	$5.6 \cdot 10^2$
S2	80	$2.5 \cdot 10^4$	$9.0 \cdot 10^6$	0.9	$1.1 \cdot 10^4$
AGN	-	-	10^{10}	1.0	$1.2 \cdot 10^7$

Table 2: Source parameters: radius R and effective temperature T_{eff} of stellar sources S1 and S2, luminosity L_{bol} of localized sources, anisotropy γ and finally radiation energy density u given in relation to $u_{\text{ISRF}} = 8.64 \cdot 10^{-14} \text{ J m}^{-3}$. The distance to the localized sources S1, S2 and AGN, is taken to be 1 pc.

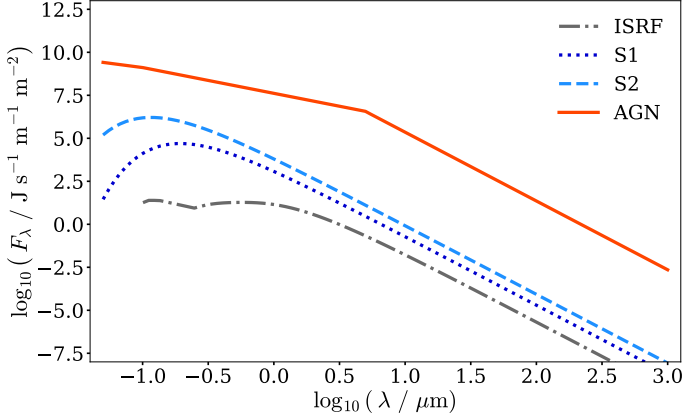


Fig. 2: Spectral flux of sources ISRF, S1, S2, and AGN, respectively, utilized to irradiate the grain aggregates.

two O-type stars labeled S1 and S2, respectively, with a flux of

$$F_{\lambda} = \pi \frac{R^2}{d^2} B_{\lambda} \quad , \quad (9)$$

where R is the stellar radius and d is the distance from the star (1 pc). The emission of an active galactic nucleus (AGN) is modeled as

$$L_{\lambda}^{\text{AGN}} = \frac{C}{\lambda} \cdot \begin{cases} 6.3 \cdot 10^{-4} & \text{if } 0.01 \mu\text{m} < \lambda \leq 0.1 \mu\text{m} , \\ 2 \cdot 10^{-4} \left(\frac{\lambda}{1 \mu\text{m}}\right)^{-0.5} & \text{if } 0.1 \mu\text{m} < \lambda \leq 5 \mu\text{m} , \\ 0.011 \left(\frac{\lambda}{1 \mu\text{m}}\right)^{-3} & \text{otherwise} , \end{cases} \quad (10)$$

following Giang et al. (2022) and Nenkova et al. (2008), where C is a constant chosen such that the integration of L_{λ}^{AGN} equals a typical AGN bolometric luminosity of $L_{\text{bol}} = 10^{10} L_{\odot}$. Finally, the spectral flux of the interstellar radiation field (ISRF) is parameterized as

$$F_{\lambda}^{\text{ISRF}} = 4\pi \begin{cases} 0 & \text{if } \lambda \leq 0.0912 \mu\text{m} , \\ 3069 \left(\frac{\lambda}{1 \mu\text{m}}\right)^{3.4172} & \text{if } 0.0912 \mu\text{m} < \lambda \leq 0.11 \mu\text{m} , \\ 1.627 & \text{if } 0.11 \mu\text{m} < \lambda \leq 0.134 \mu\text{m} , \\ 0.0566 \left(\frac{\lambda}{1 \mu\text{m}}\right)^{-1.6678} & \text{if } 0.134 \mu\text{m} < \lambda \leq 0.25 \mu\text{m} , \\ 10^{-14} B_{\lambda}(7500\text{K}) + \\ 10^{-13} B_{\lambda}(4000\text{K}) + \\ 4 \cdot 10^{-13} B_{\lambda}(3000\text{K}) & \text{otherwise} , \end{cases}$$

(11)

following Camps et al. (2015), based on Mathis et al. (1983) and Weingartner & Draine (2001). The applied parameters of the radiation sources are listed in Tab. 2 and the resulting spectral flux of the sources is shown in Fig. 2.

5. Optical and mechanical dust properties

To test the predictions of the RAT theory (Lazarian & Hoang 2007; Hoang et al. 2014) we consider silicates (SC) and carbonaceous (CA) grains, typical materials present in the ISM (see e.g. Andersson 2015, for review). The optical properties of the materials are represented by the wavelength-dependent complex refractive index $\tilde{n} = n + ik$. With n being the real part describing refraction of light interacting with the dust grain and the imaginary part k governs the light attenuation. For the SC take the (Astro)silicate model data as presented in Draine & Lee (1984); Laor & Draine (1993) and the optical properties of hydrogenated amorphous carbon are outlined in Jones (2012)². Ice mantles were not considered here, as high intensity radiation environments would not allow them. Assuming condensation of all ice species at a temperature above 150 K (Zhang et al. 2015) and comparing with dust temperatures in Tab. 3, we would expect ice-free grains for the AGN source and for CA grains around the stellar sources. The ice-free assumption may therefore generally not be valid for the ISRF and SC grains around the stellar sources. Additionally comparing with these dust temperatures assumes there is no significant difference in dust temperature when a icy surface is considered instead of the silicate/carbonaceous surface.

The radiative torque efficiency Q_{Γ} is calculated using the DDA code DDSCAT (version 7.3.3, see Draine & Flatau 1994, 2008; Flatau & Draine 2012). The grain aggregates are initialized and tabulated as outlined in Sect. 2. To create input shape-files for DDSCAT simulations, the volume enclosed by the monomers is filled with a cubic 3D-grid, each grid point representing a distinct dipole, with properties determined by the complex refractive index. DDSCAT calculations of Q_{Γ} are performed in the external coordinate system $\{\hat{e}_1, \hat{e}_2, \hat{e}_3\}$, of incoming radiation

$$Q_{\Gamma}(\theta) = Q_{e1}(\theta) \hat{e}_1 + Q_{e2}(\theta) \hat{e}_2 + Q_{e3}(\theta) \hat{e}_3 \quad , \quad (12)$$

where \hat{e}_1 is anti-parallel to the wave-vector of incoming light. For simplicity, we assume that the grain is aligned with the direction of radiation i.e. $\theta = 0^\circ$. Subsequently, the direction of radiation and rotation coincide ($\hat{e}_1 \parallel \hat{a}_1$) and the RAT efficiency factor becomes $Q_{\Gamma} \equiv Q_{e1}(\theta) \hat{e}_1$.

Simulation results are averaged over 21 equidistant values of the rotation angle of the grain around \hat{a}_1 . The results are computed for 50 wavelengths between $0.05 \mu\text{m}$ and $150 \mu\text{m}$ within equidistant bins in log-space. Each combination of material, monomer-density, size, and shape (see Sect. 2) is simulated with five different resolutions i.e. the separation of two nearest dipoles. Those are combined using an average weighted by dipole resolution. In addition to the RAT efficiency factor Q_{Γ} , DDSCAT also provides the efficiency of absorption Q_{abs} required to evaluate the photon-drag-timescale τ_{IR} and the dust

² In detail: The refractive indices of the CA material is taken from <http://vizier.cds.unistra.fr/viz-bin/VizieR?source=J/A+A/542/A98> for 30 nm hydrocarbon particles with $E_g = 2.67 \text{ eV}$ and the SC-data is listed as `eps_Sil` in <https://www.astro.princeton.edu/~draine/dust/dust.diel.html>

temperature T_{dust} . The gas-torque-efficiency Q_{gas} needed to evaluate the gas-drag-timescale τ_{gas} is calculated with a Monte Carlo (MC) based gas-dust collision approach as outlined in Reissl et al. (2022). The corresponding gas parameters³ are listed in Tab. 1.

6. Results

6.1. Drag timescales

Resulting timescales for the gas-drag and the photon-drag, respectively, taking different gas densities and dust temperatures are shown in Fig. 3. The gas-drag-timescale τ_{gas} is presented in the left panel as an average of SC and CA materials. We emphasize that the gas-drag-efficiency Q_{gas} is only dependent on grain shape in our modelling and is independent of material. We see that denser gas equals a smaller τ_{gas} in agreement with the literature (see e.g. Draine & Weingartner 1997 and Reissl et al. 2023). The dependence on monomer-density is marginal, with the BA grains having a stronger gas-drag than the BAM1 and BAM2 grains. This is due to the dependence of Q_{gas} on the surface area.

In detail, the BA grains present a larger surface area for interaction with gas particles. Following Eq.5, the expected size dependence of τ_{gas} would be linear ($I_{\text{max}} \propto a_{\text{eff}}^5$). However it is almost constant above 100 nm, which is due to Q_{gas} increasing linearly with size. In principle the gas drag efficiency Q_{gas} should only depend on the shape of the grain and not the size. That Q_{gas} nonetheless increases with size may be explained by a_{eff} not being well suited to describe grain size in this situation. The calculation of Q_{gas} uses the simulated gas-drag-torque, which depends on the angular momentum lost by the grain when a gas particle leaves the surface. This in turn scales linearly with the distance from the axis of rotation of the grain from where the gas particle is ejected. For porous grains this distance is larger than a_{eff} . The torque simulated in this way contains the information about the true shape of the grain, however, in the formula for Q_{gas} the size a_{eff} is used, which creates the size dependence of Q_{gas} .

The photon-drag-timescale is shown in the middle for SC grains and on the right for CA grains in Fig. 3. As the efficiency of absorption Q_{abs} is overall larger for SC, more photons are absorbed and emitted causing a stronger photon-drag. The number of emitted photons also depends on dust temperature, with hotter dust experiencing stronger drag (see also Tab. 3). The dependence on monomer-density is marginal, and is related to the fact that the moment of inertia being larger in the case of BA grains than for the more compact BAM2 grains given the same effective radius (see Appendix A in Reissl et al. 2023).

6.2. Torque efficiency

As we assume that the grains principal axis \hat{a}_1 is parallel to \hat{e}_1 , the direction of incoming radiation, only the Q_1 component needs to be evaluated to get the total torque efficiency Q_{Γ} . Results of the efficiency Q_{Γ} calculated with DDSCAT may possess positive (negative) values dependent on wavelength (see Fig. 4) corresponding to a direction of the angular velocity ω_{RAT}

being parallel (anti-parallel) to \hat{e}_1 . Hence, different wavelength regimes create opposing torques on the grain aggregates. Subsequently, taking the sign change into account may considerably diminish the net RAT for individual aggregates. In order to evaluate the average efficiency for different grain aggregates we both evaluate Γ_{RAT} over λ (see Eq. 1) for each grain individually including cancelling effects of positive and negative spectral contribution of $Q_{\Gamma}(\lambda)$ as well as calculate Γ_{RAT} using the absolute value $|Q_{\Gamma}(\lambda)|$, which ignores the opposing spectral contributions to the net RAT. We find that averaging over the DDSCAT data with the absolute value of $|Q_{\Gamma}|$ results only in marginally higher RATs compared to taking the sign of Q_{Γ} into account. We emphasize that the difference is insignificant compared to the variation between individual grain shapes. Hence, we utilize only the absolute value $|Q_{\Gamma}|$ in the following analysis, to make it possible to combine data of different grain shapes.

The resulting dependence of the magnitude of Q_{Γ} on wavelength for CA/BA and SC/BA grains is presented in Fig. 5. The values of Q_{Γ} are compared with the refractive index of the corresponding grain material. We report a feature for SC at $\lambda > 8 \mu\text{m}$, that follow the form of the imaginary part k of the refractive index. This feature of SC is also noted in previous studies (see e.g. LH07).

6.3. Parameterization for the RAT efficiency

Since RATs depend on the wavelength λ relative to the grain radius a_{eff} it is convenient to evaluate $|Q_{\Gamma}|$ as a function of λ/a_{eff} (see Fig. 6) instead of λ alone. Here, the slopes of the different grain sizes overlap tightly, showing the self-similar nature that allowed the canonical parametrization (Eq. 2) for solid grains in the first place. Our results using grain aggregates shows a comparable constant part for $\lambda/a_{\text{eff}} < 1.8$, but do not follow the overall power-law parametrization for $\lambda/a_{\text{eff}} > 1.8$. Instead both materials SC and CA, reveal a steeper power-law that overlaps for all sizes from $\lambda/a_{\text{eff}} \approx 3$ and then goes over into a shallower power-law for $\lambda/a_{\text{eff}} \gtrsim 10$. A similar behavior of a broken power-law can be seen in previous studies e.g. in LH07 or for gaussian dust grains in Herranen et al. (2019), but is much more apparent here. Consequently, we suggest a modified parameterization for ballistic grain aggregates with two connected consecutive power-laws. Least square fits for the constant part (called c in this study) and the two power-laws are performed for all data points of the grains sharing the same material and monomer-density. The fits of c are performed for individual grain sizes in the interval $\lambda/a_{\text{eff}} < 3$. All sizes are fitted jointly for the first and second power-law with exponents q_1 and q_2 in the intervals $3 < (\lambda/a_{\text{eff}}) < 12$ and $(\lambda/a_{\text{eff}}) > 20$. In practice the power-laws are fitted as linear functions to the logarithm of the data.

In order to combine the three regions conveniently into a continuous curve the following definition was chosen:

$$|Q_{\Gamma}| = \begin{cases} c(a_{\text{eff}}) & \text{if } \left(\frac{\lambda}{a_{\text{eff}}}\right) \leq a, \\ c\left(\frac{\lambda}{a_{\text{eff}}}/a\right)^{q_1} & \text{if } a \leq \left(\frac{\lambda}{a_{\text{eff}}}\right) \leq b, \\ c\left(\frac{b}{a}\right)^{q_1} \left(\frac{\lambda}{a_{\text{eff}}}/b\right)^{q_2} & \text{otherwise.} \end{cases} \quad (13)$$

Here, the individual fits are joined by calculating the intersection points a and b , where a is the intersection of c with the steep power-law and b is the one of both power-laws. Therefore like c , there will be a different value of a for each a_{eff} . The resulting parametrization is shown in Fig. 7 for the exemplary data set of carbon BA-grains of size 200 nm. All resulting fit parameters of Eq. 13 are given in Appendix A.

³ We note that the gas number density n_{gas} is lower than in a typical AGN torus. However, we can position the dust grain outside the torus, selecting a position in which n_{gas} is similar to the ISM, e.g. at higher inclinations from the plane of the torus.

source	CA			SC		
	T_{\min} [K]	T_{mean} [K]	T_{\max} [K]	T_{\min} [K]	T_{mean} [K]	T_{\max} [K]
AGN	780	925	1164	312	375	484
S2	274	302	343	81	91	106
S1	186	197	212	45	49	55
ISRF	72	79	88	15	16	18

Table 3: Range of the resulting dust temperatures T_{dust} considering SC and CA materials and the different source AGN, S1, S2, and ISRF, respectively.

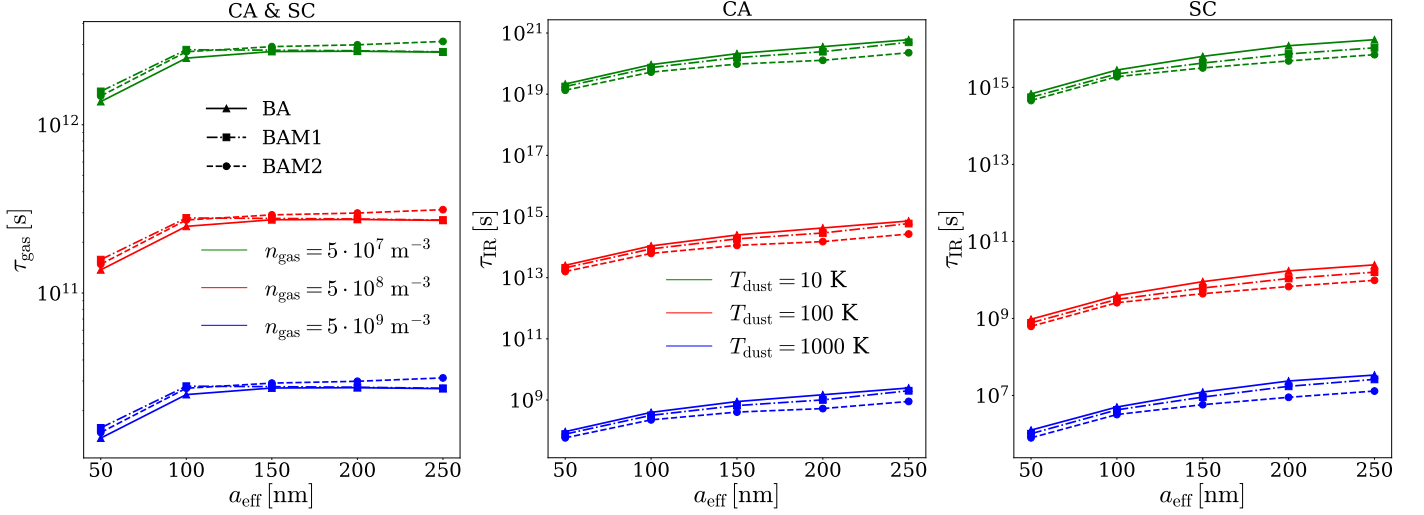


Fig. 3: *Left panel:* The drag timescales over the effective radius a_{eff} dependent on grain model (BA, BAM1, BAM2) and different gas densities n_{gas} for all grain materials. Here, the gas temperature is at a constant value of $T_{\text{gas}} = 100$ K. *Center panel:* The same as the left panel but for the IR drag timescale for the CA grain material, for different dust temperatures T_{dust} . *Right panel:* The same as center panel but for the SC grain material.

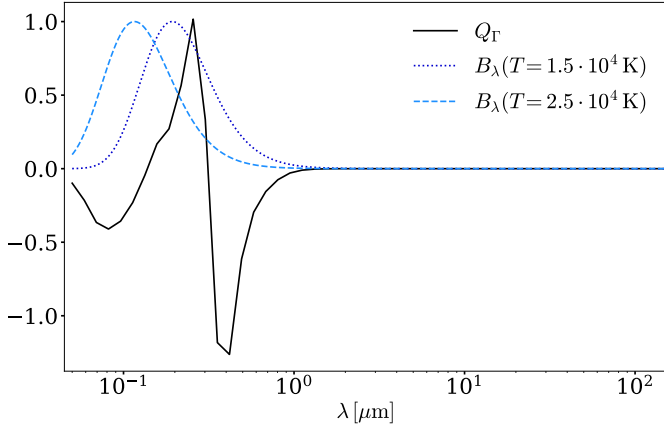


Fig. 4: Torque efficiency Q_{Γ} as a function of wavelength λ for an exemplary CA/BA grain of size $a_{\text{eff}} = 200$ nm. The spectra of the two stellar sources S1 and S2, respectively, are shown in blue, normalized by their maximum value. We emphasize that this particular grain has two changes in sign resulting in a reduced net-torque over wavelengths.

Larger grains interact more efficiently with the radiation field resulting in a higher value c as can be seen in Fig. 6. The BAM1 and BAM2 grain models have comparable curves for $|Q_{\Gamma}|$, where

the values differ most in the constant part on a scale similar to the difference between two grain sizes. The more porous the grain the larger c . Differences between the two materials are the values of c , which are larger for SC. Both power-laws are steeper for CA, most likely due to interference by the feature in the SC material.

6.4. Net torques and angular velocities

The exact difference in RAT using the canonical or the modified parameterization and, subsequently, the magnitude of the angular velocity of the grains cannot a priori be quantified due to the dependency of RATs on the spectral characteristics of the radiation field. Therefore we calculate the maximal angular velocity ω_{RAT} induced by RATs using both parameterizations and compare the results to those we get using the DDSCAT data of individual grains.

If the torque efficiency $Q_{\Gamma}(\lambda)$ for a single grain exhibits some sign changes over wavelength (see Fig. 4), this leads to a lower torque overall as different wavelengths exert RAT components in opposite directions. As mentioned above, the effect of positive and negative components of Q_{Γ} cancelling out appears to be small compared to the overall variation in the strength of Q_{Γ} between different grains. The torque along \hat{a}_1 is calculated for each grain following Eq. 1, where Q_{Γ} is used without taking the absolute value. Then, the maximal angular velocity is calculated

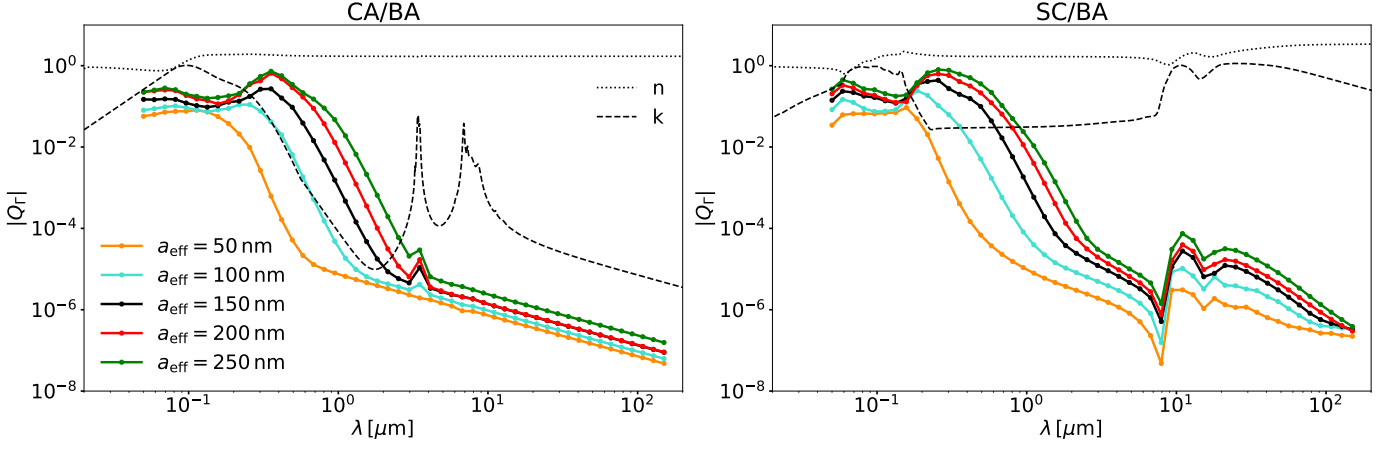


Fig. 5: Average torque efficiency $|Q_T|$ over wavelengths for CA (left) and SC (right) BA-aggregates of different grain sizes a_{eff} (color coded) in comparison with the real part n (dotted line) and imaginary part k (dashed line) of the corresponding refractive indices. We note that characteristic features of Q_T follow the shape of k .

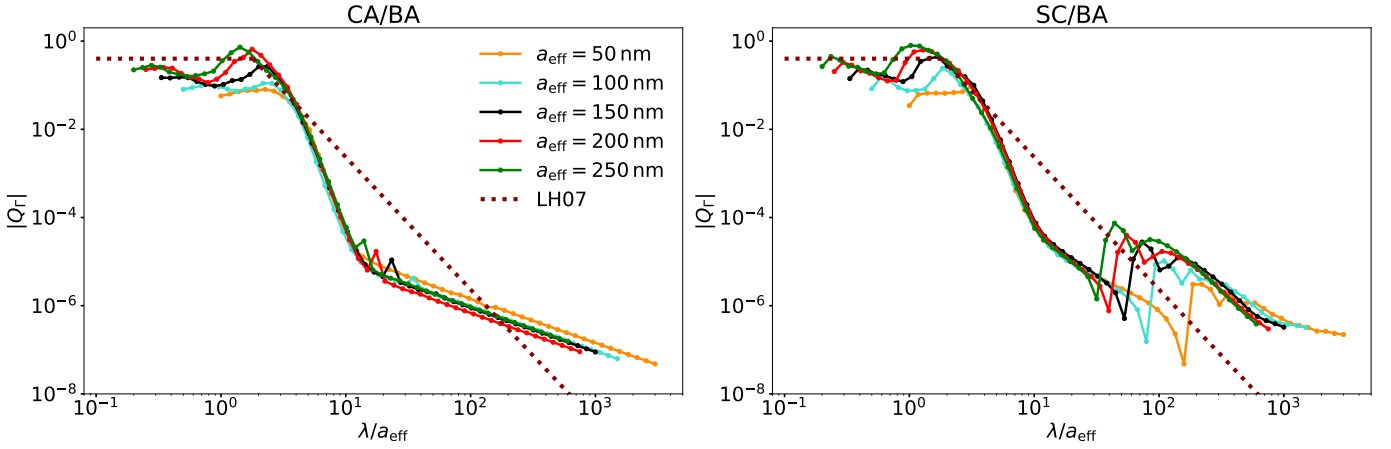


Fig. 6: The same as Fig. 5 but for the average torque efficiency Q_T over λ/a_{eff} in comparison with the conical power-law parametrization (red dotted line) as suggested in LH07.

with Eq. 3, where τ_{drag} and I_{max} are also evaluated individually for each grain.

Figure 8 shows the distribution of angular velocities and torques for individual CA/BA grains and the most luminous source i.e. the AGN. The distributions are broken down by grain size. We report that the resulting values of the RATs may span a range up to two orders of magnitude, with a larger spread below the mean. The mean of the distribution increases with grains size, as larger grains have higher Q_T values in the constant part. The distributions of the different grain sizes are more distinct in Γ_{RAT} and overlap significantly for ω_{RAT} , due to the influence of the drag timescale (see Eq. 3).

Using a parametrization describing the average value for an ensemble of grains saves the need to calculate ω_{RAT} for every single grain. We therefore compare the average values obtained from individual grain calculations (shown in Fig. 8 as solid lines) with the values obtained when using the canonical parametrization for Q_T (dotted lines). This parametrization does not model the means of the distributions well. It overestimate the values of Γ_{RAT} and ω_{RAT} , especially for the smaller grains.

To quantify how the canonical parametrization of LH07 and the modified parametrization of our study compare with the distribution means for all combinations of radiation sources, materials, and monomer-densities, we show the distribution means of

the RATs in Fig. 9 as a function the grain size a_{eff} . The CA material in the left column, the SC material in the right column, the monomer-densities in the rows and the four radiation sources are shown with different colours in each panel. The difference between the sources is due to the linear dependence of Γ_{RAT} with energy density u and anisotropy factor γ where more efficient RATs are reached for stronger radiation sources (see Eq. 1 and Tab. 2).

In Fig. 10 we present the mean angular velocities ω_{RAT} corresponding to the RATs shown in Fig. 9. Here, the variations of ω_{RAT} between individual sources is different to the one of Γ_{RAT} , because ω_{RAT} also depends on τ_{drag} , which itself depends indirectly on u via the temperature dependence of τ_{IR} . Using the dust temperatures in Tab. 3 one can estimate τ_{IR} for the given temperature from Fig. 3. The gas drag timescale is independent of u and about $\tau_{\text{gas}} \gtrsim 10^{12}$ s for the chosen gas density of $n_{\text{gas}} = 5 \cdot 10^7 \text{ m}^{-3}$. We can see, that the drag timescale is dominated by τ_{gas} for the low dust temperatures of the ISRF source, both timescales are about equal for S1 and τ_{IR} dominates for S2 and AGN, where the dust is the hottest.

Therefore, the difference in ω_{RAT} depends only on u and γ for the ISRF, but is dominated by τ_{IR} for the other radiation sources. This is why the three stronger sources are much closer in ω_{RAT} than in Γ_{RAT} . The difference in τ_{IR} between the two ma-

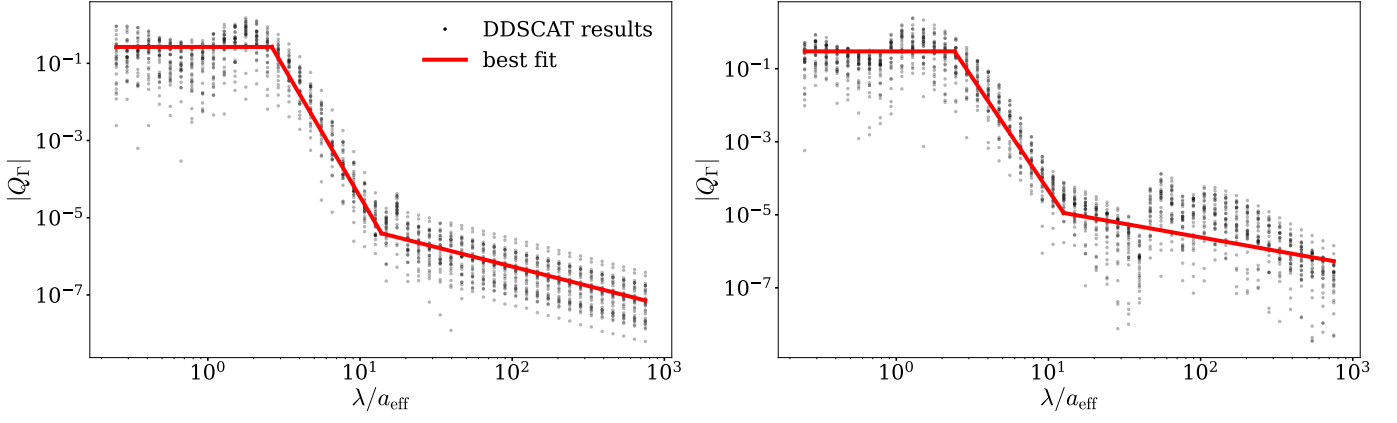


Fig. 7: Two-power law parametrization shown as a red line for CA (left) and SC (right) BA-grains in comparison with the full set of the numerical DDSCAT simulations (black dots) for grains of size $a_{\text{eff}} = 200$ nm where the absolute value of the torque efficiency $|Q_T|$ are plotted as a function of λ/a_{eff} . The constant part c is fitted for each grain size up to a value of $\lambda/a_{\text{eff}} = 3$, the steeper power-law is fitted as a linear function to the logarithm of the data for all sizes combined in the interval $3 < \lambda/a_{\text{eff}} < 10$, same for the shallow power-law in the interval $\lambda/a_{\text{eff}} > 20$. Finally, the two intersection points a and b are calculated and used to create a continuous parametrization for $|Q_T|$ (see Eq. 13).

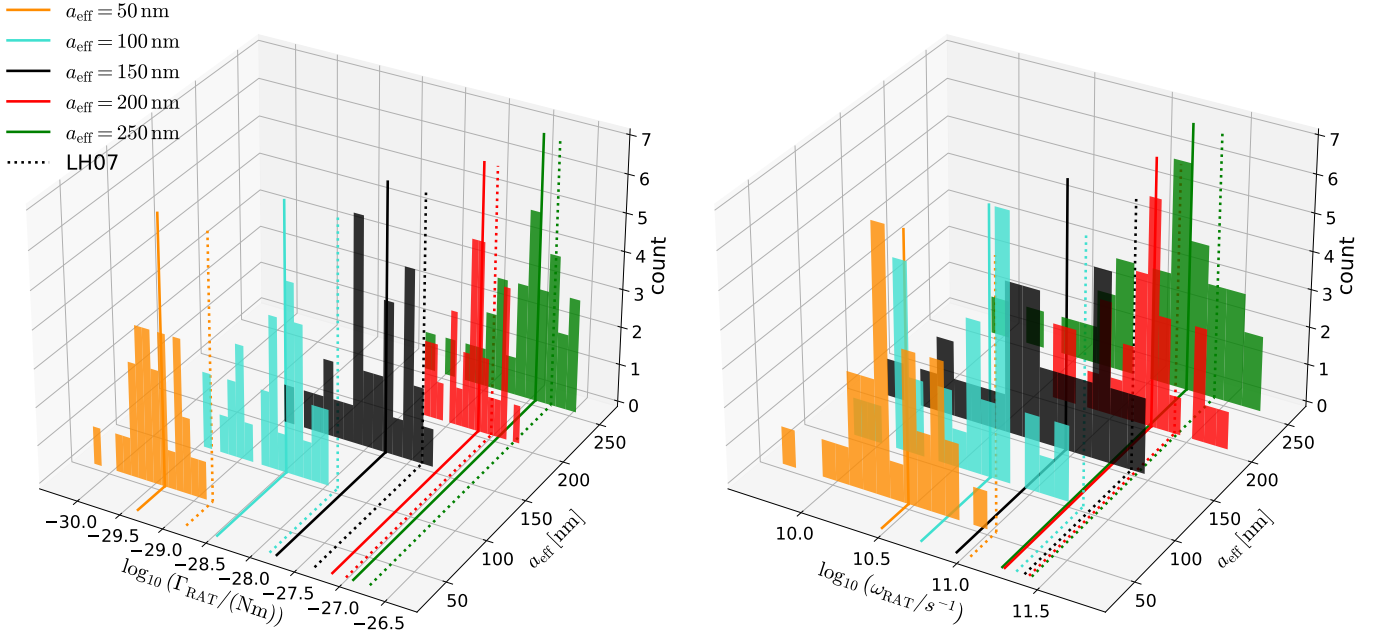


Fig. 8: Histograms representing the distribution of the RAT Γ_{RAT} (left) and angular velocity ω_{RAT} (right) for CA/BA grains of different grain sizes showing and the AGN as radiation source. Continuous lines show the mean for each distribution, dotted lines show the value calculated using the canonical parametrization (LH07). Mean values for ω_{RAT} are calculated from the mean values of Γ_{RAT} shown in the lower panel as well as averages for τ_{drag} and I_{max} . We note that RATs by the canonical parametrization are consistently higher than the mean values of the dust aggregates.

terials thereby also leads to smaller angular velocity for S1, S2 and AGN for SC compared to CA, but no difference between the two materials for ISRF, as τ_{gas} dominates there. The difference between monomer-densities is a decrease in Γ_{RAT} from BA to BAM2 smaller than one order of magnitude, due to Q_T decreasing with monomer-density. The resulting decrease with monomer-density in ω_{RAT} is smaller, due to I_{max} also decreasing with monomer-density.

As expected RATs have a strong scaling with a_{eff} and it does not change much between sources, materials and monomer-densities. However, for the angular velocity ω_{RAT} , the results are

less uniform as shown in Fig. 10. Here, there is no scaling with grain size for the ISRF source, and a weak one for the other sources, which flattens towards the larger grains for SC and even declines for CA with the S1 source. We remark that the scaling of ω_{RAT} with grain size depends on the interplay between multiple factors: spectrum of the source, magnitude of the drag timescale, which depends on the material and size of the grain, and whether τ_{IR} or τ_{gas} dominates for the given environment. It thereby differs from the scaling in other publications e.g. Hoang et al. (2019).

The canonical parametrization gives more accurate results for

the larger grains, as they experience the strongest torques. We point out that overall the canonical parametrization overestimates the mean ω_{RAT} , with differences up to one order of magnitude. In comparison, the two-power-law parametrization resembles the mean of the DDSCAT data more precisely and performs equally well for all sources, materials, monomer-densities, and sizes.

A way to quantify the efficiency of RATs of porous aggregates was proposed by Tatsuuma & Kataoka (2021), TK21 hereafter. The TK21 parametrization takes the porosity (monomer-density) of the grain aggregates into account via the volume filling factor ϕ , where $\phi = 1$ represents a solid grain and $\phi = 0$ represents completely empty space. Here, the volume filling factor ϕ is added into the canonical parametrization as follows

$$|Q_{\Gamma}| = \begin{cases} 0.4 & \text{if } \lambda \leq 1.8a_{\text{eff}} \times \phi, \\ 0.4 \left(\frac{\lambda}{1.8a_{\text{eff}} \times \phi} \right)^{\alpha} & \text{otherwise.} \end{cases} \quad (14)$$

Fig. 11 shows the average angular velocity ω_{RAT} in comparison with the TK21 parametrization and canonical parametrization of LH07. The proposed parametrization of TK21 tends to overestimate the resulting ω_{RAT} as well, especially for the stronger radiation sources, but clearly improves upon the canonical parametrization of LH07. As shown in Fig. 11, merely introducing ϕ to take the grain porosity into account cannot improve the agreement between our results and the canonical parametrization considerably indicating that complex grain shapes differ in their interaction with radiation compared to compact grains in more fundamental ways than just by making the grains porous.

Consequently, using the two-power-law parametrization of Q_{Γ} to calculate the average ω_{RAT} for an ensemble of ballistic grain aggregates is the most accurate choice even though individual grains may have larger or much smaller ω_{RAT} by several orders of magnitude (see Fig. 8), due to random variation in grain shape.

7. Discussion and Caveats

An underlying assumption in our RAT calculations using grain aggregates is the anisotropy of incoming radiation. As DDSCAT only simulates anisotropic radiation, we used the anisotropy factor γ to treat a certain percentage of the source radiation as anisotropic. For instance a grain in a molecular cloud around a forming star receives a portion γ of the stellar radiation directly (anisotropically) and the rest isotropically due to scattering on surrounding particles. Such processes are not fully accounted for in this work, however, we do not expect torques from isotropic radiation to dominate torques from anisotropic radiation, especially for our grain model with no variations of optical properties across the grains surface.

We also assume perfect alignment of the grain rotation axis with the direction of the radiation i.e. $\theta = 0$. This is based on the fact, that grains preferentially align with the direction of incoming radiation in the absence of magnetic fields (see LH07). Though in general magnetic fields might be present and the grains may not reach suprathermal angular velocities. For a more detailed picture, one would need DDSCAT simulations sampling the whole range of θ -angles. These can then be used to calculate phase space trajectories of grains in θ and ω , possibly including magnetic fields. Such an approach may allow to verify if the assumption of fixed orientation was justified, and if not, to gauge

how large the deviation is. However, this is beyond the scope of our current study.

Using a parametrization to model the average angular velocity is still possible with the more detailed grain model, even including positive and negative values of $Q_{\Gamma}(\lambda)$ for individual grains. If needed it might also be possible to parametrize the distribution of ω_{RAT} values (see Fig. 8), or other quantities using larger grain ensembles.

As we were limited to a small range of grain sizes due to the computational restrictions of DDSCAT, future simulation setups should be designed to test if the two-power-law parametrization for $|Q_{\Gamma}|$ also holds for larger grains. If this is the case and the two-power-law shape is also seen for general orientations of the grain, it would stand to reason, that the form of $|Q_{\Gamma}|$ following two power-laws is intrinsic to the nature of grains composed of monomers, like the single power-law of the canonical parametrization is for compact grains. It might be convenient to generalize the parameters of the parametrization and give them a functional form dependent on monomer-density and grain size. Fig. 12 shows the constant part c of the parametrization as a function of grain size for different monomer-densities. We can see that the linear increase of c with grain size has a different slope for each monomer-density, with the slope roughly doubling from BAM2 to BAM1 and tripling from BAM2 to BA. It is therefore possible, that for each material there is a functional form of c as a linear function with the slope depending on monomer-density. To see if and how the exponents q_1 and q_2 depend on material or monomer-density would require a larger sample of monomer-densities and refractive indices (materials).

We have shown, that aggregated grains have a different functional form of $Q_{\Gamma}(\lambda)$ than compact grains and therefore do not reach as high angular velocities as compact grains would in the same circumstances, with differences of up to an order of magnitude for the smallest grains. However we see that our results and the canonical parametrization agree for the least dense and largest grains (BA, 250 nm). If the trend of increasing c for larger grain size and lower monomer-density (see Fig. 12) holds true, we would expect Γ_{RAT} to further increase for less dense and larger grains. That lower monomer-density leads to higher torques makes intuitive sense considering it increases the total surface area of the grain and therefore the cross section for interaction with radiation just as increasing the grain size does. While the torque increases, ω_{RAT} however does not increase further for larger grains and in some cases even decreases again for the largest grains. Aggregate grains larger than the ones simulated here may potentially not reach much higher angular velocities, as the drag also increases with size.

How much ω_{RAT} increases for higher radiation energy densities strongly depends on the optical properties and therefore on the composition of the grains, due to different drag-effects dominating in different environments. The significantly increased surface area and more complex geometry of aggregated grains has to be taken into account.

The dust grains were assumed to have no relative velocity to the gas, but it is possible, that grains close to strong radiation fields experiencing linear acceleration by the radiation pressure will reach high drift velocities relative to the surrounding gas. The rotation of the grain would then also be influenced by mechanical torques (Reissl et al. 2022) working in a similar way to RATs, with gas collisions instead of photon collisions.

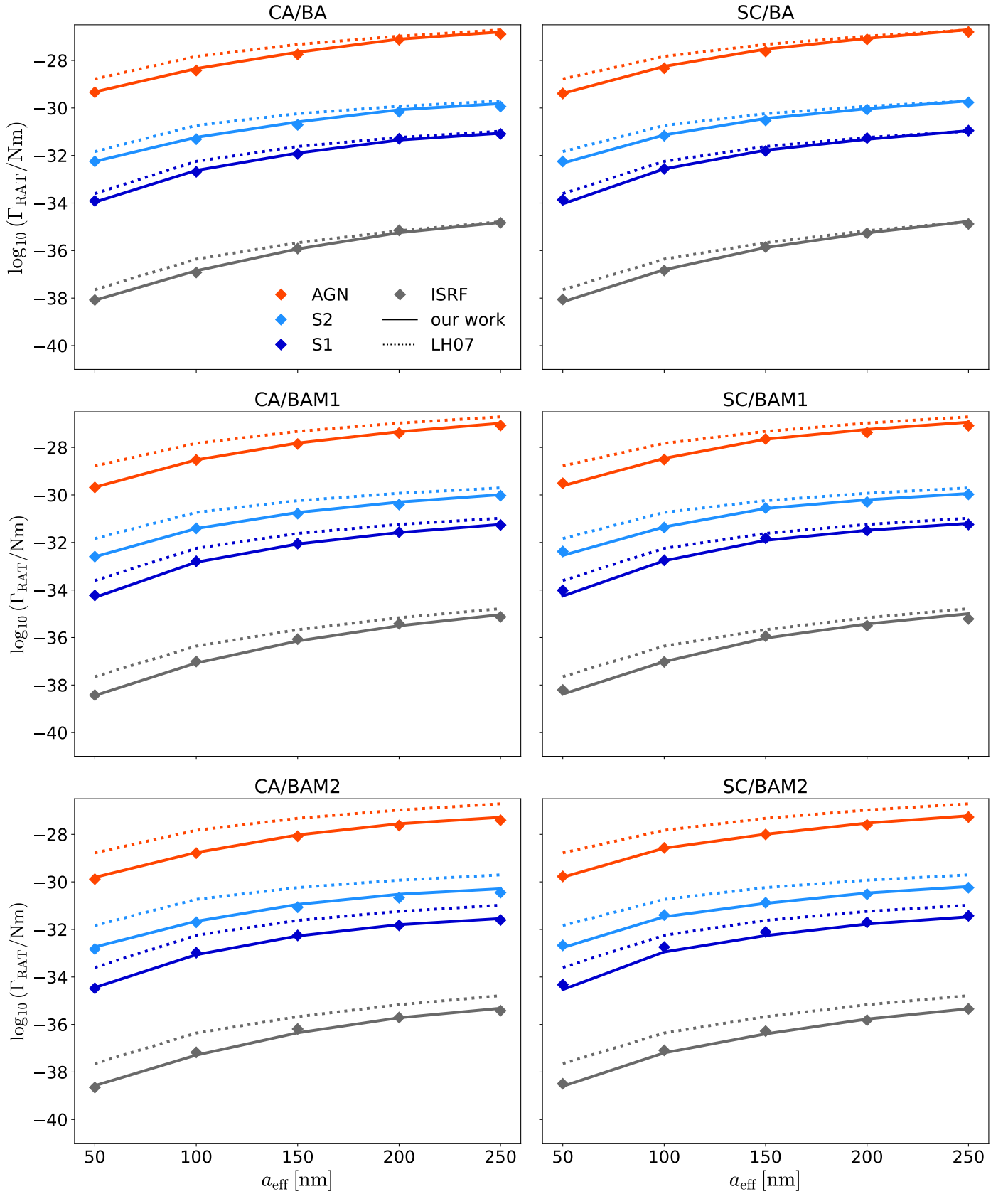


Fig. 9: The RATs Γ_{RAT} (solid line) per grain size a_{eff} calculated with the two-power-law parametrization is shown in comparison to the RATs predicted by the canonical parametrization suggested in LH07 (dotted line) as well as the average of the DDSCAT simulation data (diamonds). Each color represents one of the different sources i.e. ISRF (grey), S1 (dark blue), S2 (light blue), or AGN (red), respectively, utilizing the CA grain material (left column) and the SC material (right column) with monomer-densities BA (top row), BAM (middle row), or BAM2 (bottom row). This figure is to be compared with Fig. 8.

8. Summary and Outlook

In this paper, we present a numerical study of the impact of grain shape on the radiative torque (RAT) alignment efficiency. This particular alignment mechanism predicts a sensitivity of the grain alignment efficiency with respect to the magnitude of the radiation field as well as the materials and shape of the dust grains. As a source of radiation we consider O-type stars, an active galactic nuclei (AGN) and the interstellar radiation field (ISRF) typical for the Milky Way. The dust grains are modelled by means of ballistic aggregation and migration (BAM) of monomers of various sizes. The aggregation process is biased to control the size and number of connections of the grain aggregates. We calculate the optical dust grain properties in the discrete dipole approximation using the DDCAT code considering the refractive indices of pure carbonaceous and silicate grains, respectively. Given the optical properties of the dust aggregates and the radiation energy density we calculate the maximal angular velocity ω_{RAT} according to RAT alignment theory assuming stable alignment. Our major findings are as follows:

- We report that the ISRF produced average angular velocities $\omega_{\text{RAT}} = 10^6 \text{ s}^{-1}$ for both carbon and silicate grains where as the O-type stars and AGN sources produced much larger ω_{RAT} in a range of 10^9 s^{-1} to 10^{11} s^{-1} for carbon grains and 10^8 s^{-1} to 10^{10} s^{-1} for silicate grains.
- Compared to the O-type stars, for the AGN the angular velocity ω_{RAT} of grains did not increase in a similar manner, as photon emission drag forces on the grains increase. This is because of higher dust temperatures in the AGN environment.
- Considering an entire ensemble of BAM grain aggregates, we propose a new parametrization for the RAT efficiency that follows a broken power law with a constant part for shorter wavelengths followed by two distinct power laws to cover longer wavelengths. The proposed parametrization describes the average angular velocities ω_{RAT} reached by the ensembles of grains more precisely, than the canonical parametrization derived for compact grains.
- According to our DDSCAT calculations individual grain aggregates may have sign changes in the RAT efficiency over the entire wavelength regime reducing the net torque integrated over wavelength. However, the appearance of such sign changes does impact the average grain spin-up behaviour of the entire ensemble only marginally.

Our results for a parametrization with two power-laws for grains composed of monomers, potentially improved by expanding to a parametrization for the distribution of ω_{RAT} values, can make detailed studies on grain rotation including grain size, porosity, and material easier by replacing computationally expensive DDSCAT simulations of individual grains. The assumption of unobscured source radiation may be dropped by including effects of the surrounding gas and dust around the grain to better gauge the effect of RATs further away from the radiation source or in dense environments. Furthermore, the results of this work may be further constrained by including a general rotation of the grains, possibly including magnetic fields, where individual grains are followed along their pathways in the rotation phase-space.

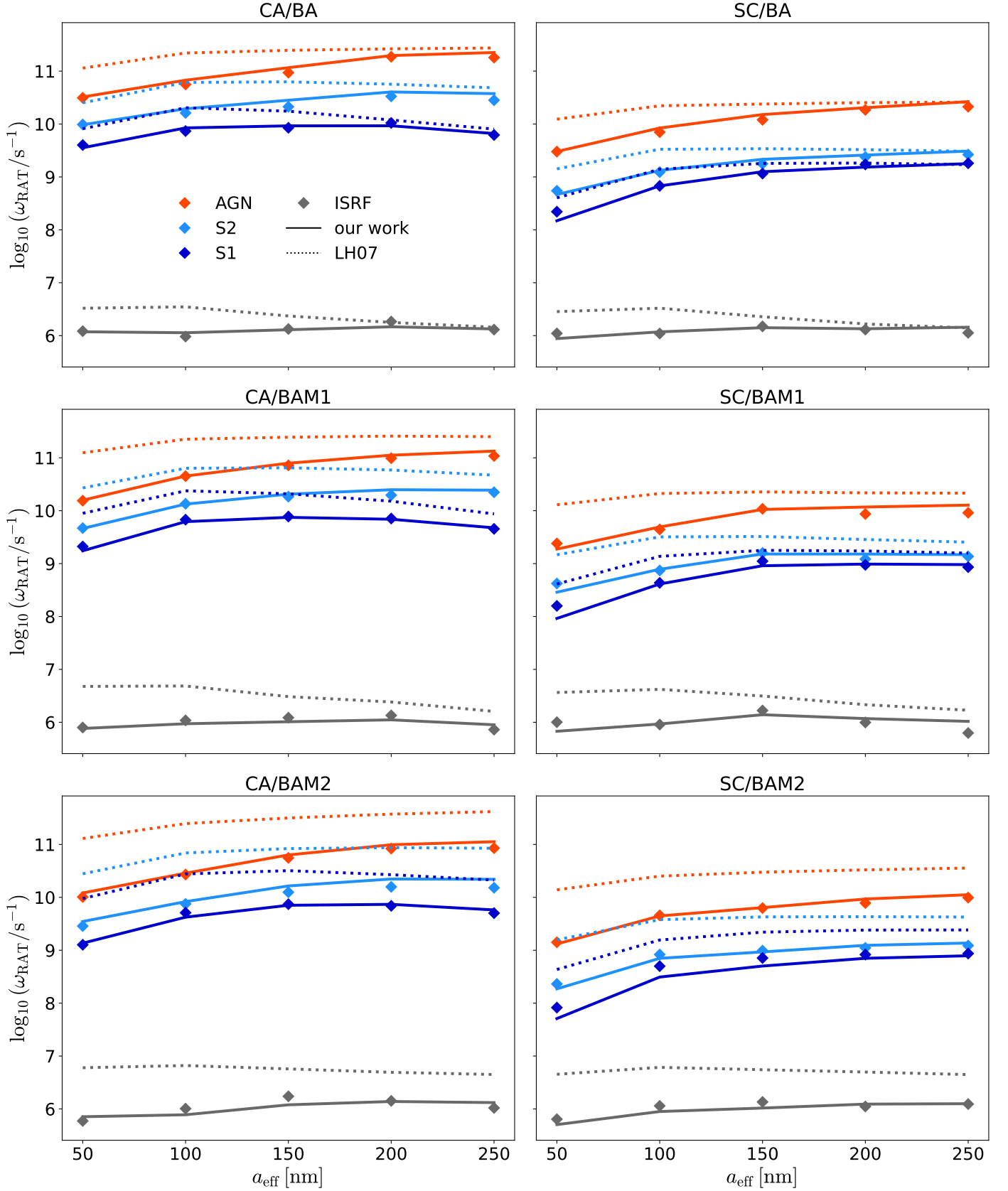


Fig. 10: Same as Fig. 9 but for angular velocity ω_{RAT} . We emphasize that the canonical parameterization may overpredict the magnitude of ω_{RAT} up to one order of magnitude higher for BAM grain aggregates as the two-power-law parameterization.

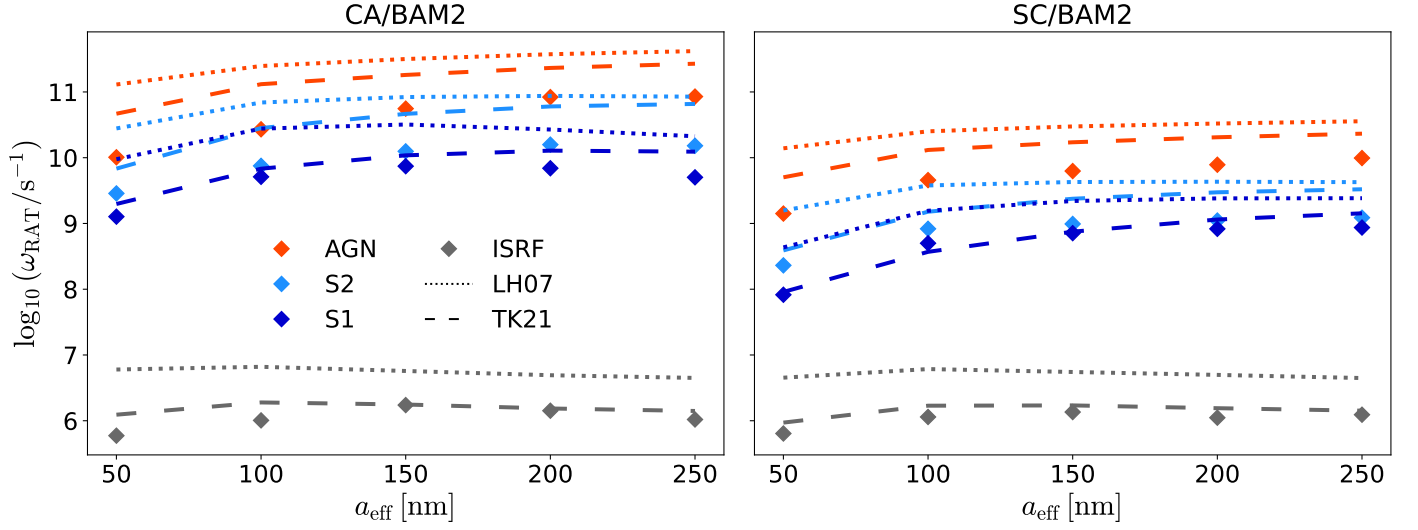


Fig. 11: The same as Fig. 10 but only for CA/BAM2 (left panel) and SC/BAM2 (right panel) grain aggregates showing the canonical parametrization of LH07 (dotted lines) in comparison with the parametrization for porous grains suggested in TK21 (dashed lines).

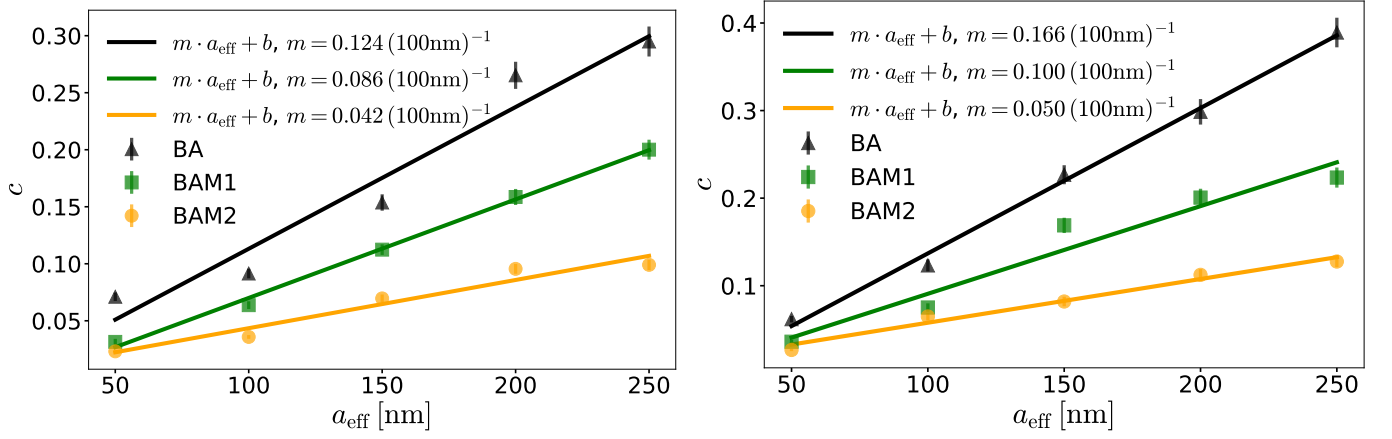


Fig. 12: Constant part of two-power-law parametrization c vs. grain size for CA (left) and SC (right), dotted lines show linear regression for each grain model.

Appendix A: Two power-law parametrization fit parameters

For completeness we provide the full set of fitted parameters of the two-power-law RAT parametrization in table A.1 for CA grains and in table A.2 for SC grains.

Acknowledgements. Special thanks go to Thiem Hoang for numerous enlightening discussion. S.R., J.A.J., and R.S.K. acknowledge financial support from the Heidelberg cluster of excellence (EXC 2181 - 390900948) “*STRUCTURES: A unifying approach to emergent phenomena in the physical world, mathematics, and complex data*”, specifically via the exploratory project EP 4.4. S.R. and R.S.K. also thank for support from Deutsche Forschungsgemeinschaft (DFG) via the Collaborative Research Center (SFB 881, Project-ID 138713538) ‘The Milky Way System’ (subprojects A01, A06, B01, B02, and B08). And we thank for funding from the European Research Council in the ERC synergy grant “*ECOGAL – Understanding our Galactic ecosystem: From the disk of the Milky Way to the formation sites of stars and planets*” (project ID 855130). The project made use of computing resources provided by *The Länd* through bwHPC and by DFG through grant INST 35/1134-1 FUGG. Data are in part stored at SDS@hd supported by the Ministry of Science, Research and the Arts and by DFG through grant INST 35/1314-1 FUGG.

References

- Andersson, B. G. 2015, in *Astrophysics and Space Science Library*, Vol. 407, *Magnetic Fields in Diffuse Media*, ed. A. Lazarian, E. M. de Gouveia Dal Pino, & C. Melioli, 59
- Arnold, J. A., Weinberger, A. J., Videen, G., & Zubko, E. S. 2019, *The Astrophysical Journal*, 157, 157, publisher: The American Astronomical Society
- Barnett, S. J. 1917, 10, 7, ADS Bibcode: 1917PhRv...10....7B
- Bernstein, R. A., Freedman, W. L., & Madore, B. F. 2002, 571, 107
- Bethell, T. J., Chepurinov, A., Lazarian, A., & Kim, J. 2007, *The Astrophysical Journal*, 663, 1055, aDS Bibcode: 2007ApJ...663.1055B
- Calzetti, D., Armus, L., Bohlin, R. C., et al. 2000, *The Astrophysical Journal*, 533, 682, publisher: IOP ADS Bibcode: 2000ApJ...533..682C
- Camps, P., Misselt, K., Bianchi, S., et al. 2015, A&A, 580, A87
- Cazaux, S., & Tielens, A. G. G. M. 2002, 575, L29
- Davis, L., & Greenstein, J. L. 1951, 114, 206, ADS Bibcode: 1951ApJ...114..206D
- Dishoeck, E. F. v. 2014, 168, 9, publisher: Royal Society of Chemistry
- Dolginov, A. Z. 1972, *Astrophysics and Space Science*, 18, 337
- Dolginov, A. Z. & Mytrophanov, I. G. 1976, *Astrophysics and Space Science*, 43, 291
- Dominik, C. & Tielens, A. G. G. M. 1997, *ApJ*, 480, 647
- Draine, B. T. 2003, *Annual Review of Astronomy and Astrophysics*, 41, 241, publisher: Annual Reviews
- Draine, B. T. & Flatau, P. J. 1994, *J. Opt. Soc. Am. A*, 11, 1491
- Draine, B. T. & Flatau, P. J. 2008, 25, 2693, publisher: Optica Publishing Group
- Draine, B. T. & Lee, H. M. 1984, *ApJ*, 285, 89
- Draine, B. T. & Weingartner, J. C. 1996, *ApJ*, 470, 551
- Draine, B. T. & Weingartner, J. C. 1997, *The Astrophysical Journal*, 480, 633
- Draine, B. T. & Weingartner, J. C. 1997, *ApJ*, 480, 633
- Dullemond, C. P., Brauer, F., Henning, T., & Natta, A. 2008, 2008, 014015
- Flatau, P. J. & Draine, B. T. 2012, 20, 1247, publisher: Optica Publishing Group
- Giang, N. C., Hoang, T., Tram, L. N., et al. 2022, *ApJ*, 936, 108
- Gobrecht, D., Cherchneff, I., Sarangi, A., Plane, J. M. C., & Bromley, S. T. 2016, *Astronomy & Astrophysics*, 585, A6, publisher: EDP Sciences
- Gold, T. 1952, 169, 322, number: 4295 Publisher: Nature Publishing Group
- Goodman, A. A., Jones, T. J., Lada, E. A., & Myers, P. C. 1995, 448, 748, ADS Bibcode: 1995ApJ...448..748G
- Harwit, M. & Vanýsek, V. 1971, *Bulletin of the Astronomical Institutes of Czechoslovakia*, 22, 18, aDS Bibcode: 1971BAICz...22...18H
- Herranen, J., Lazarian, A., & Hoang, T. 2019, *The Astrophysical Journal*, 878, 96, publisher: The American Astronomical Society
- Hoang, T. & Lazarian, A. 2008, *Monthly Notices of the Royal Astronomical Society*, 388, 117, aDS Bibcode: 2008MNRAS.388..117H
- Hoang, T. & Lazarian, A. 2009, *The Astrophysical Journal*, 695, 1457, aDS Bibcode: 2009ApJ...695.1457H
- Hoang, T. & Lazarian, A. 2014, *Monthly Notices of the Royal Astronomical Society*, 438, 680, aDS Bibcode: 2014MNRAS.438..680H
- Hoang, T. & Lazarian, A. 2016, *The Astrophysical Journal*, 831, 159, aDS Bibcode: 2016ApJ...831..159H
- Hoang, T., Lazarian, A., & Martin, P. G. 2014, *ApJ*, 790, 6
- Hoang, T. & Tram, L. N. 2020, *ApJ*, 891, 38
- Hoang, T., Tram, L. N., Lee, H., & Ahn, S.-H. 2019, *Nature Astronomy*, 3, 766
- Hollenbach, D. & Salpeter, E. E. 1971, 163, 155, ADS Bibcode: 1971ApJ...163..155H
- Johnson, K. L., Kendall, K., & Roberts, A. D. 1971, *Proceedings of the Royal Society of London Series A*, 324, 301
- Jones, A. P. 2012, *Astronomy & Astrophysics*, 540, A2, publisher: EDP Sciences
- Laor, A. & Draine, B. T. 1993, *The Astrophysical Journal*, 402, 441, aDS Bibcode: 1993ApJ...402..441L
- Lazarian, A. 2007, *J. Quant. Spectr. Rad. Transf.*, 106, 225
- Lazarian, A. & Hoang, T. 2007, *Monthly Notices of the Royal Astronomical Society*, 378, 910
- Lazarian, A. & Hoang, T. 2008, *ApJ*, 676, L25
- Liu, B. & Ji, J. 2020, 20, 164, publisher: National Astronomical Observatories, CAS and IOP Publishing Ltd.
- Mathis, J. S., Mezger, P. G., & Panagia, N. 1983, *Astronomy and Astrophysics*, 128, 212, aDS Bibcode: 1983A&A...128..212M
- Nanni, A., Bressan, A., Marigo, P., & Girardi, L. 2013, *Monthly Notices of the Royal Astronomical Society*, 434, 2390, aDS Bibcode: 2013MNRAS.434.2390N
- Neenkova, M., Sirocky, M. M., Ivezić, Z., & Elitzur, M. 2008, *The Astrophysical Journal*, 685, 147, publisher: IOP Publishing
- Norris, B. R. M., Tuthill, P. G., Ireland, M. J., et al. 2012, *Nature*, 484, 220, number: 7393 Publisher: Nature Publishing Group
- Omukai, K., Tsuribe, T., Schneider, R., & Ferrara, A. 2005, *The Astrophysical Journal*, 626, 627
- Planck Collaboration, Aghanim, N., Akrami, Y., et al. 2020, *Astronomy and Astrophysics*, 641, A12, aDS Bibcode: 2020A&A...641A..12P
- Purcell, E. M. 1979, 231, 404, ADS Bibcode: 1979ApJ...231..404P
- Reissl, S., Meehan, P., & Klessen, R. S. 2022, arXiv e-prints, arXiv:2201.03694
- Reissl, S., Nguyen, P., Jordan, L. M., & Klessen, R. S. 2023, arXiv e-prints, arXiv:2301.12889
- Reissl, S., Wolf, S., & Brauer, R. 2016, *Astronomy & Astrophysics*, 593, A87, publisher: EDP Sciences
- Schneider, R., Valiante, R., Ventura, P., et al. 2014, *Monthly Notices of the Royal Astronomical Society*, 442, 1440, aDS Bibcode: 2014MNRAS.442.1440S
- Shen, Y., Draine, B. T., & Johnson, E. T. 2008, *ApJ*, 689, 260
- Tatsuuma, M. & Kataoka, A. 2021, *The Astrophysical Journal*, 913, 132
- Todini, P. & Ferrara, A. 2001, *Monthly Notices of the Royal Astronomical Society*, 325, 726, aDS Bibcode: 2001MNRAS.325..726T
- Weingartner, J. C. & Draine, B. T. 2001, *The Astrophysical Journal Supplement Series*, 134, 263, aDS Bibcode: 2001ApJS..134..263W
- Zhang, K., Blake, G. A., & Bergin, E. A. 2015, *The Astrophysical Journal Letters*, 806, L7, publisher: The American Astronomical Society

monomer-density	q_1	q_2	b	a_{eff} [nm]	c	a
BA	-6.690 ± 0.007	-1.0032 ± 0.0003	14 ± 5	50	0.071 ± 0.004	3.202 ± 0.026
				100	0.091 ± 0.004	3.083 ± 0.022
				150	0.154 ± 0.007	2.853 ± 0.021
				200	0.265 ± 0.012	2.629 ± 0.018
				250	0.295 ± 0.013	2.588 ± 0.018
BAM1	-6.659 ± 0.011	-1.02855 ± 0.00022	12 ± 4	50	0.0315 ± 0.0027	3.21 ± 0.04
				100	0.064 ± 0.003	2.891 ± 0.025
				150	0.112 ± 0.005	2.655 ± 0.018
				200	0.159 ± 0.007	2.521 ± 0.018
				250	0.200 ± 0.009	2.434 ± 0.017
BAM2	-6.073 ± 0.007	-1.01848 ± 0.00018	13 ± 5	50	0.0232 ± 0.0014	3.13 ± 0.03
				100	0.0358 ± 0.0016	2.916 ± 0.023
				150	0.070 ± 0.003	2.614 ± 0.022
				200	0.096 ± 0.004	2.481 ± 0.019
				250	0.099 ± 0.005	2.467 ± 0.019

Table A.1: Parameters for CA

monomer-density	q_1	q_2	b	a_{eff} [nm]	c	a
BA	-6.168 ± 0.008	-0.7434 ± 0.0004	13 ± 5	50	0.062 ± 0.004	3.11 ± 0.03
				100	0.123 ± 0.007	2.785 ± 0.026
				150	0.227 ± 0.011	2.523 ± 0.020
				200	0.299 ± 0.015	2.412 ± 0.020
				250	0.389 ± 0.017	2.311 ± 0.017
BAM1	-6.393 ± 0.007	-0.7033 ± 0.0003	12 ± 4	50	0.0360 ± 0.0022	3.18 ± 0.03
				100	0.075 ± 0.005	2.832 ± 0.029
				150	0.169 ± 0.009	2.494 ± 0.021
				200	0.201 ± 0.010	2.428 ± 0.020
				250	0.224 ± 0.011	2.387 ± 0.020
BAM2	-5.386 ± 0.008	-0.8477 ± 0.0003	11 ± 5	50	0.0266 ± 0.0014	2.779 ± 0.027
				100	0.065 ± 0.004	2.36 ± 0.03
				150	0.082 ± 0.005	2.256 ± 0.028
				200	0.112 ± 0.007	2.127 ± 0.023
				250	0.128 ± 0.006	2.078 ± 0.020

Table A.2: Parameters for SC